

USIGAN: Unbalanced Self-Information Feature Transport for Weakly Paired Image IHC Virtual Staining

Yue Peng[†], Bing Xiong[†], Fuqiang Chen, Deboch Eybo Abera, RanRan Zhang, Wanming Hu, Jing Cai, Wenjian Qin*

Abstract—Immunohistochemical (IHC) virtual staining is a task that generates virtual IHC images from H&E images while maintaining pathological semantic consistency with adjacent slices. This task aims to achieve cross-domain mapping between morphological structures and staining patterns through generative models, providing an efficient and cost-effective solution for pathological analysis. However, under weakly paired conditions, spatial heterogeneity between adjacent slices presents significant challenges. This can lead to inaccurate one-to-many mappings and generate results that are inconsistent with the pathological semantics of adjacent slices. To address this issue, we propose a novel unbalanced self-information feature transport for IHC virtual staining, named USIGAN, which extracts global morphological semantics without relying on positional correspondence. By removing weakly paired terms in the joint marginal distribution, we effectively mitigate the impact of weak pairing on joint distributions, thereby significantly improving the content consistency and pathological semantic consistency of the generated results. Moreover, we design the Unbalanced Optimal Transport Consistency (UOT-CTM) mechanism and the Pathology Self-Correspondence (PC-SCM) mechanism to construct correlation matrices between H&E and generated IHC in image-level and real IHC and generated IHC image sets in intra-group level. Experiments conducted on two publicly available datasets demonstrate that our method achieves superior performance across multiple clinically significant metrics, such as IoD and Pearson-R correlation, demonstrating better clinical relevance. The code is available at: <https://github.com/MIXAILAB/USIGAN>

Index Terms—Histopathology, Virtual Stain, Unbalanced Optimal Transport, Self Information Mining

I. INTRODUCTION

IMMUNOHISTOCHEMISTRY (IHC) virtual staining is a task that aims to generate virtual IHC images consistent with the pathological semantics of adjacent reference IHC-stained slices while preserving the content consistency of H&E images. However, spatial heterogeneity between adjacent slices makes it challenging to directly establish a mapping between H&E and IHC images. In previous studies, most researchers adopted contrastive learning approaches, which maximize mutual information in the corresponding regions to establish cross-domain correlations between the morphological

information in H&E images and the staining styles in IHC images. However, this approach still fails to address the issue of spatial heterogeneity, which can lead to misalignment of morphological information from H&E images to incorrect IHC staining patterns, affecting the extraction and accurate mapping of key information in generative models [21, 13, 25]. Therefore, we focus on a previously overlooked concept in information theory—self-information, which quantifies the information content of a single event. Specifically, self-information reflects the rarity of a pixel. For example, when rare structures or patterns appear in pathological images, the corresponding regions exhibit higher self-information, indicating that they contain more valuable diagnostic information and biological significance. In summary, self-information quantifies the model’s prioritization of information needs for critical pathological features.

Our goal is to transform self-information from a previously passive learning paradigm into an active focus, further uncovering the process by which generative models establish cross-domain correlations in virtual staining. Self-information represents critical regions in the mapping process, and constructing a correlation matrix allows different feature regions to be assigned higher weights, which is the essence of self-information mining. As illustrated in Figure 1, IHC virtual staining faces two main challenges: (1) spatial heterogeneity and (2) erroneous pathological semantic correlations caused by incorrect one-to-many mappings between morphological features and staining patterns. Self-information mining addresses these challenges by prioritizing key information. We leverage two types of priors in virtual staining to incorporate corresponding self-information and establish correlations: 1) Explicit Prior: Pathological semantic consistency between adjacent slices. By evaluating staining intensity through clinical optical density metrics, we construct a correlation matrix between generated IHC and real IHC image groups to mine pathological semantic self-information. 2) Implicit Prior: Morphological structures and cellular atypia in H&E images correspond to different disease subtypes and their respective IHC staining patterns [14]. Through optimal transport theory, we optimize the expectation of self-information, explicitly introducing self-information to strengthen critical regions and penalizing the effects of erroneous one-to-many mappings.

In previous studies on IHC virtual staining, two paradigms: fully supervised and unsupervised—have been primarily used to passively construct cross-domain correlations. Pix2Pix and its variants attempt to establish cross-domain correlations at the pixel level by leveraging weakly paired IHC data [8,

[†] Yue Peng and Bing Xiong contribute equally to this work.

* Wenjian Qin are corresponding author to this work.

B. Xiong, Y. Peng, F. Chen, Deboch, Abera, R. Zhang are with the ShenZhen Institutes of Advanced Technology, university chinese academy of sciences, ShenZhen, China, 518055. Email: wj.qin@siat.ac.cn.

W. Hu are with Department of Pathology, Sun Yat-sen University Cancer Center, State Key Laboratory of Oncology in South China, Guangdong Provincial Clinical Research Center for Cancer, Guangzhou 510060, China

J. Cai are with Department of Health Technology and Informatics, The Hong Kong Polytechnic University, Hong Kong 999077, China

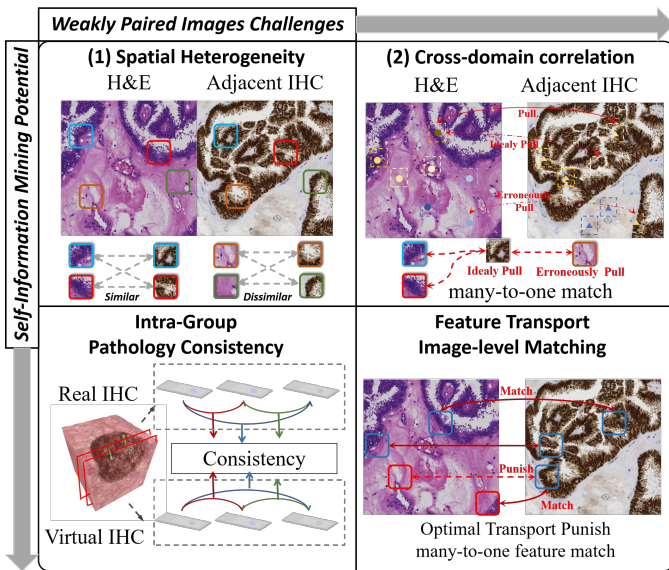


Fig. 1. Spatial heterogeneity between adjacent slices poses a major challenge in virtual staining. This heterogeneity manifests as misalignment of tissue structures and pathological semantics across slices, making it difficult to directly establish cross-domain mappings between morphology and staining styles.

19, 6, 23]. However, these methods struggle to effectively learn mapping relationships between tissue regions. Cycle consistency-based methods implicitly construct mappings between morphology and staining styles by allowing two models to map between two domains [31]. However, the assumption of reciprocal mappings between staining domains is often violated for weakly paired data, resulting in low pathological semantic consistency in the generated results. To address these issues, some researchers have adopted contrastive learning approaches that maximize mutual information between patches to explicitly construct mapping relationships [8, 19, 6, 23]. While this non-pixel-level approach alleviates the impact of weakly paired data to some extent, its performance remains constrained by the degree of pairing. These methods overlook the critical role of self-information in pathological images. Passively summarizing mapping relationships from image collections is inherently challenging, whereas self-information, by emphasizing features with high diagnostic value, can guide the model to correctly focus on key regions, thereby improving the performance and consistency of virtual staining results.

In this paper, we propose a novel method for mining self-information at both the image and group levels by eliminating weakly paired terms in the joint marginal distribution, effectively mitigating their impact and significantly enhancing the content and pathological semantic consistency of generated results. Specifically, for image-level self-information mining, we introduce Unbalanced Optimal Transport Consistency Mining (UOT-CTM), a method that preserves geometric structures of high self-information regions to reduce transport costs during optimal transport minimization. Although previous attempts using optimal transport explicitly constrained transport plans from H&E to weakly paired IHC and from generated IHC to weakly paired IHC in feature space—thus aligning morpho-

logical and staining style features—these approaches suffer from three primary limitations: 1) Neglecting incompatibility in weakly paired data, leading to forced, low-similarity feature matching. 2) Ignoring inherent semantic differences between morphological and staining-style imitation tasks, resulting in undesirable trade-offs. 3) Overlooking semantic inconsistencies and distributional differences by directly constraining joint marginal distributions involving weakly paired terms. To address these issues, UOT-CTM employs a cyclic consistent transport strategy to explicitly constrain transport plans along paths from H&E to generated IHC, effectively capturing image-level self-information. Additionally, we propose a marginally relaxed unbalanced optimal transport strategy to alleviate the one-to-many mapping issue and construct more accurate correlation matrices, transforming the constraint objective from directly matching $P(x, y)$ and $P(y, z)$ distributions to matching $P(x, z)$ and $P(x, y) \cdot P(y, z)$, thus eliminating weakly paired terms. For group-level self-information mining, we design the Pathology-Consistent Self-Correspondence Mining (PC-SCM) mechanism, which leverages optical density—rare but indicative of high self-information—as a “self-information anchor,” establishing correlation matrices between generated and real IHC based on optical density. This ensures prioritization of high-optical-density regions, maintains consistent correlation matrices within batches, avoids negative impacts from directly using weakly paired IHC as learning templates, and effectively captures pathological semantic information. Our contributions can be concluded as follows:

- We introduce the concept of self-information of the image in histopathology. By maximizing this self-information, we achieve a marked boost in cross-domain correlation accuracy, delivering virtual IHC results that are superior in both content and pathological semantic consistency.
- To mine image-level self-information we employ unbalanced optimal transport, which mitigates the adverse effects of flawed one-to-many mappings through feature-matching transport.
- We develop a self-information anchor via optical density feature to guide intra-batch self-information mining, while avoiding the impact of its spatial heterogeneity on morphological information.

II. RELATED WORK

A. Image-to-Image Translation

The task of image translation aims to map images from a source domain to a target domain while preserving their original content [26, 10, 7, 24]. Pix2Pix used a patch-based discriminator on paired data to alleviate the tendency of previous generative models toward style averaging [8], establishing itself as a cornerstone method in supervised image translation. Subsequent supervised methods introduced various extensions, such as cross-layer connections for high-resolution generation and perceptual constraints [23]. However, due to its strict requirement for pixel-level paired data, Pix2Pix is difficult to generalize to broader applications. CycleGAN [31] introduced a framework based on the bidirectional mapping hypothesis and cycle consistency loss, which became the foundation for

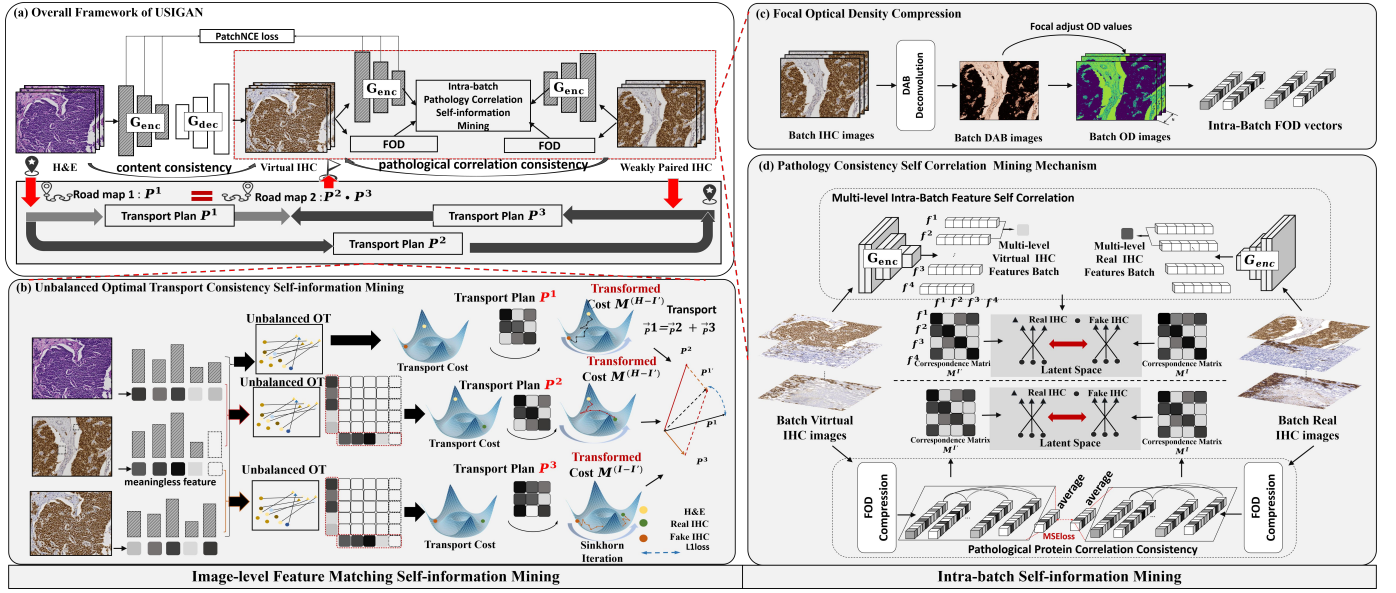


Fig. 2. We leverage weakly paired IHC as an intermediate bridge to ensure global consistency between H&E and IHC while mining image-level self-information through a transport consistency framework. Simultaneously, we utilize focal optical density and DAB deconvolution to extract optical density feature vectors to guide intra-batch self-information mining. Multi-scale features within the batch are used as auxiliary features to fully explore intra-batch self-information.

subsequent methods. To address the overly strict bidirectional mapping assumption of cycle consistency, CUT [4], based on contrastive learning, constructs cross-domain correlations using positive and negative patch samples. Contrastive learning-based image translation methods grounded in optimal transport theory have also garnered significant attention.

Although existing image translation methods show great potential in pathological image stain transfer, the lower coupling between content and style in pathological images, along with the higher demand for content consistency [25], makes it challenging for these methods to accurately generate virtual images that maintain both pathological features and content consistency.

B. Immunohistochemical Virtual Staining

Immunohistochemical virtual staining aims to generate staining results for specific protein markers from source-stained images while preserving image content. This technique is gaining increasing attention in digital pathology. DoanNgan et al. proposed an IHC virtual staining method that generates Ki67 protein markers from fluorescence images, demonstrating a certain mapping relationship between morphological information and positive signals. However, its reliance on paired data makes it challenging to implement in clinical applications [3]. Zhang et al. proposed an IHC multi-staining mapping method that measures the accuracy of specific protein markers based on mean intensity optical density (MIOD), introducing a novel evaluation metric for assessing the molecular response accuracy of virtual staining results [28]. Liu et al. proposed a method that annotates positive regions in breast tissue H&E images to achieve high pathological correlation with adjacent slice labels, further demonstrating that morphological information can effectively

distinguish positive regions [16]. Chen et al., on the other hand, sought to reduce the demand for labeled positive signal data by using DAB deconvolution for destaining, segmenting positive regions based on optical density thresholds, and employing an additional feature extractor to refine pseudo-labels [1], thereby achieving high preservation of pathological semantics. However, this method heavily relies on the quality of the feature extractor, which limits its practicality. It is evident that the morphological information in H&E images plays a crucial role in maintaining pathological relevance.

In addition, the weak pairing caused by spatial heterogeneity between adjacent slices has also drawn researchers' attention. Liu et al. proposed using fuzzy labels to alleviate pixel-level misalignment issues [15]. However, since the differences between adjacent slices are far greater than those caused by spatial displacement, the generated results often lose important high-frequency information. Guan et al. proposed leveraging pathological correlations across batches to mitigate weak pairing and achieved remarkable results [5]. However, this method overlooks the critical role of morphological information in H&E images for positive signals and may encounter discrepancies in the "total quantity" of positive signals between weakly paired data, leading to excessive positive signal expression in the generated results.

III. METHOD

A. Image-level Self-information Mining

Self-information, as a measure of the information content of a specific event, has its expectation represented by entropy. To mine self-information, we adopt the optimal transport strategy, which, like self-information, effectively describes differences in probability distributions. Classical optimal transport aims to determine the minimal total cost of moving one measure

to another, where the "cost" is evaluated by the transportation distance multiplied by the transported mass. Entropy, as the expectation of self-information, is introduced through the entropy regularization term in optimal transport to measure the complexity of information. This enables the image to identify key features through global matching rather than relying on positional correspondence to maximize mutual information for establishing cross-domain correlations. Under the constraint of limited total transportation mass, optimal transport effectively penalizes many-to-one matching relationships, thereby alleviating the issue of many-to-one mapping between specific protein responses and morphological features caused by the erroneous minimization of local mutual information during contrastive learning in weakly paired data for cross-domain correlation construction. We define the feature which is encoded from H&E(X) and IHC(Y) image alignment as an optimal transport problem and derive the constraints of total masses. It can be formulated as the following:

$$\min_{\pi \in \Pi(p, q)} \int_{X \times Y} c(x, y) \pi(x, y) dx dy \quad (1)$$

where $\pi(x, y)$ is the transport plan with $\pi \geq 0$. $c(x, y)$ is the transport cost function, which can be defined $C_{ij} = -\frac{x_i^T \cdot y_j}{\|x_i\| \|y_j\|}$. x_i and y_j is locations feature vectors of X and Y. $\Pi(p, q)$ is the set of joint distributions with fixed.

$$\Pi(p, q) = \left\{ \pi \geq 0 : \begin{cases} \int_Y \pi(x, y) dy = p(x), \\ \int_X \pi(x, y) dx = q(y) \end{cases} \right\} \quad (2)$$

where $p(x)$ and $q(y)$ are the source and target distributions. However, classical optimal transport has strict constraints, as it can only handle distributions with equal total mass. When the total mass of the source distribution $p(x)$ and the target distribution $q(y)$ is inconsistent (i.e., $\int p(x) dx \neq \int q(y) dy$), classical optimal transport (OT) enforces mass matching: if $p(x) > q(y)$ (the source distribution has greater total mass), OT splits the mass of a single source point and distributes it to multiple target points; if $p(x) < q(y)$ (the target distribution has greater total mass), OT merges the mass of multiple source points and assigns it to a single target point, resulting in many-to-one mapping [27]. In weakly paired data, the assumption of equal feature mass is often difficult to satisfy, rendering the penalty mechanism for many-to-one mapping based on optimal transport physically meaningless. Furthermore, some feature points are forcibly matched to target points with dissimilar features, leading to inaccurate mappings.

To validate my hypothesis, I employed a ResNet50 backbone pre-trained on natural images to extract features from H&E images and weakly paired IHC images, followed by t-SNE for feature dimensionality reduction. When the two feature sets satisfy the optimal transport (OT) assumption, there should be a certain correspondence between the source and target distributions, implying some shared mass (overlapping regions). In this case, t-SNE should not completely separate the two feature sets. However, as shown in the Figure 9, the features of H&E images and weakly paired IHC images

exhibit entirely disjoint distributions, indicating no shared patterns between them. This makes it challenging for OT to establish a reasonable mass mapping path. Under such circumstances, where the H&E and IHC feature distributions are completely separated, OT results may become unstable or even unreasonable. For instance, OT may forcibly map the source distribution's mass to distant regions of the target distribution, incurring high transport costs. Alternatively, OT may overly rely on regularization (e.g., entropy regularization) to "smooth" such unreasonable mappings, potentially rendering the mapping results meaningless.

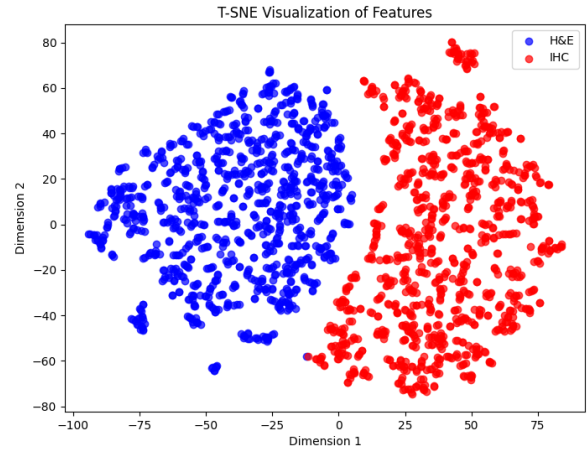


Fig. 3. The features extracted from H&E images and weakly paired IHC data using a pre-trained ResNet exhibit significant distribution differences, making it challenging to satisfy the mass conservation assumption of classical OT methods.

Therefore, we introduce a relaxed version of classical optimal transport theory, called unbalanced optimal transport [2], which aims to determine the transport plan for distributions with differing masses in weakly paired data. We developed a "soft" penalty with a divergence metric to replace the "hard" mass conservation constraint in Eq 1:

$$\inf_{\pi \in \mathcal{M}_{2,+}(X \times Y)} \int_{X \times Y} c(x, y) \pi(x, y) dx dy - \epsilon H(\pi) + \tau D_{KL}(\pi_x \| p) + \tau D_{KL}(\pi_y \| q) \quad (3)$$

where $\mathcal{M}_{2,+}(X \times Y)$ is the set of all non-negative joint distributions. $D_{KL}(\pi_x \| p)$ and $D_{KL}(\pi_y \| q)$ are Kullback Leibler divergence terms. τ is the regulation parameter, which is 0 when it is classical optimal transport. $c(x, y)$ is the transport cost function, which follows the classical optimal transport. $H(\pi)$ is an entropy regularization term introduced to make the entire formulation differentiable, which can be formulated as:

$$H(\pi) = - \int_{X \times Y} \pi(x, y) \log \pi(x, y) dx dy + \|\pi\|_1 \quad (4)$$

where $\|\pi\|_1 = \int_{X \times Y} \pi(x, y) dx dy$ is the total mass of π . To solve the above problem efficiently, we consider its Fenchel-Legendre dual form, which introduces dual potentials

u and v corresponding to source and target distributions, respectively. The dual form is given as:

$$\sup_{u,v} \left[-F^*(-u) - G^*(-v) - \eta \sum_{x,y} \exp \left(\frac{u(x) + v(y) - c(x,y)}{\eta} \right) \right] \quad (5)$$

where $F^*(-u)$ and $G^*(-v)$ are the Legendre conjugates of the KL divergence terms, computed as:

$$F^*(-u) = \tau \langle e^{u/\tau}, p \rangle - \tau \langle \mathbf{1}, p \rangle \quad (6)$$

$$G^*(-v) = \tau \langle e^{v/\tau}, q \rangle - \tau \langle \mathbf{1}, q \rangle \quad (7)$$

To approximate the solution of the UOT problem, we use the Sinkhorn algorithm. The algorithm alternates between updating dual potentials u and v iteratively until convergence. The updates are given as:

$$u(x) \leftarrow -\tau \log \left(\sum_y q(y) \exp \left(\frac{v(y) - c(x,y)}{\eta} \right) \right) \quad (8)$$

$$v(y) \leftarrow -\tau \log \left(\sum_x p(x) \exp \left(\frac{u(x) - c(x,y)}{\eta} \right) \right) \quad (9)$$

Finally, the transport plan T is computed from the dual potentials as:

$$T(x,y) = p(x)q(y) \exp \left(\frac{u(x) + v(y) - c(x,y)}{\eta} \right) \quad (10)$$

We define the transport plan $T^{(H-I)}$ between H&E images and weakly paired IHC images, capturing distributional differences such as texture structure, and the transport plan T^{I-I} between generated and weakly paired IHC images, reflecting molecular expression imitation differences; we assume these two transport plans should be as similar as possible in the feature space. By minimizing the cost of the transport plan, regions with high self-information receive priority, facilitating the accurate representation of distributional relationships and semantic mappings. Specifically, given that H&E images X and weakly paired IHC images Y share morphological and structural features, we define the minimal transport cost f_1 from x_{ij} to y_{ij} ; similarly, as weakly paired IHC Y and generated IHC Z share staining type and texture features, we define f_2 from y_{ij} to z_{ij} . Consequently, an indirect transport plan $f_{\text{indirect}} = f_1 \cdot f_2$ can represent the sequential feature mapping through these two steps, while the direct transport plan f_{direct} between H&E and generated IHC images is computationally simpler due to their shared features and adherence to classical optimal transport assumptions.

$$\mathcal{L}_{\text{tcyc}} = \frac{1}{N^2} \sum_{i=1}^N \sum_{j=1}^N \left| \mathbf{T}^{(H-I)} \cdot \mathbf{T}^{(I-I)} - f_{\text{direct}} \right| \quad (11)$$

where f_{direct} represent $\mathbf{T}^{(H-\hat{I})}$, \hat{I} is virtual IHC image. Theoretically, by combining transport plans, the joint probability distribution $P(x, z)$ between H&E images and generated IHC replaces the joint probability distributions $P(x, y)$ between H&E and weakly paired IHC, and $P(y, z)$ between weakly paired IHC and generated IHC, thereby eliminating the influence of weakly paired data. The joint marginal distributions can be formulated as:

$$P(x, z) = \sum_y P(x, y) \cdot P(y, z)$$

The all transport plans are computed based on the Unbalanced Optimal Transport (UOT) method.

B. Intra-batch Self-information Mining

Optical density is an indirect indicator for assessing antibody concentration in IHC-stained images, and it serves as an important basis for clinically evaluating disease subtypes in IHC images. Optical density is highly correlated with abnormal regions in the image, where high optical density values, representing high antibody concentrations, often reflect abnormal biological expressions. Therefore, as a critical metric for evaluating pathological semantics, optical density can act as a self-information anchor to directly guide the generative model in focusing on key regions. To effectively model the pathological correlation among batch-level IHC images, first, we introduce optical density, which is proportional to the concentration of the stain [1]. The amount of stain is the factor determining the OD at a wavelength as per the LambertBeerlaw [22]. It can be formulated as:

$$OD_C = -\log_{10}(I_C/I_{0,C}) = A * c_C \quad (12)$$

where $I_{0,C}$ and I_C denote the light intensity entering and passing the specimen. We use traditional color deconvolution [20]for stain separation. Then we specifically select DAB stain's OD values to generate the RGB image (IHC DAB). Due to the high optical density (OD) values in positive regions, which are typically much smaller in area compared to negative regions, the distribution becomes unbalanced. To amplify the influence of positive regions in self-information mining, we adjust Equation 12 to assign grayscale values to positive signals using a focal calibration map, referred to as Focal Optical Density (FOD).

$$O_C = (-\log_{10}(I_C/I_{0,C}))^\alpha \quad (13)$$

where O is the FOD with tunable focusing parameter $\alpha > 1$. We convert virtual IHC and real IHC to O^F and O^R , which use ReLU to activate and flatten as vector f_i^F and f_i^R . Then we calculate the optical density relational function between any two real IHC feature within the batch to obtain correlation matrix \mathbf{M} , which can be formulated as :

$$\mathbf{M} = \begin{bmatrix} \cos(\mathbf{f}_1, \mathbf{f}_1) & \cos(\mathbf{f}_1, \mathbf{f}_2) & \cdots & \cos(\mathbf{f}_1, \mathbf{f}_n) \\ \cos(\mathbf{f}_2, \mathbf{f}_1) & \cos(\mathbf{f}_2, \mathbf{f}_2) & \cdots & \cos(\mathbf{f}_2, \mathbf{f}_n) \\ \vdots & \vdots & \ddots & \vdots \\ \cos(\mathbf{f}_n, \mathbf{f}_1) & \cos(\mathbf{f}_n, \mathbf{f}_2) & \cdots & \cos(\mathbf{f}_n, \mathbf{f}_n) \end{bmatrix}$$

where $\cos(\cdot, \cdot)$ denotes the Cosine similarity. M^R and M^F denotes real IHC and fake IHC optical density self-correlation map. Then, we propose \mathcal{L}_{odc} , which maximize the preservation of pathological correlation among batch samples. It can be formulated as:

$$\mathcal{L}_{odc} = \|M^R - M^C\| + \frac{1}{N^2} \left\| \sum_{i,j} O^R(i,j) - \sum_{i,j} O^F(i,j) \right\|_2^2 \quad (14)$$

In this module, we will adopt \mathcal{L}_{cc} for feature batches as a multi-level feature auxiliary term to assist \mathcal{L}_{odc} in mining intra-batch pathological consistency self-information. \mathcal{L}_{cc} is the the consistency between M^R and M^F , calculated based on multi-level feature cosine similarity. \mathcal{L}_{cc} , as a shorter gradient backpropagation path, influences the encoder.

$$\mathcal{L}_{cc} = \|M^R - M^F\| \quad (15)$$

C. Loss functions

The loss function term in the USI-GAN include adversial loss \mathcal{L}_{adv} , PatchNCE loss $\mathcal{L}_{patchnce}$, transport consistency loss \mathcal{L}_{tscy} , correlation consistency loss \mathcal{L}_{cc} , integrated optical density correlation consistency loss \mathcal{L}_{odc} . Adversial loss can be formulated as:

$$\mathcal{L}_{adv} = \mathbb{E}_{y \in Y} \log D(Y) + \mathbb{E}_{x \in X} \log(1 - D(X)) \quad (16)$$

where \mathbb{E} denotes the expectation, X and Y denote the source and target domain feature. G represent Generator and D represent Discriminator. PatchNCE loss \mathcal{L}_{nce} establishes cross-domain correlations by maximizing the mutual information between the input and output, which can be expressed as:

$$\mathcal{L}_{nce}(\mathbf{v}, \mathbf{v}^+, \mathbf{v}^-) = -\log \left[\frac{\exp(\mathbf{v} \cdot \mathbf{v}^+ / \tau)}{\exp(\mathbf{v} \cdot \mathbf{v}^+ / \tau) + \sum_{n=1}^N \exp(\mathbf{v} \cdot \mathbf{v}^- / \tau)} \right] \quad (17)$$

where \mathbf{v} , \mathbf{v}^+ and \mathbf{v}^- are the embeddings of the anchor, positive and negative samples, respectively, τ is a temperature hyper-parameter. The PatchNCE can be formulated as:

$$\mathcal{L}_{patchnce}(X) = \mathbb{E}_{x \in X} \sum_{l=1}^L \sum_{s=1}^{S_l} \mathcal{L}_{nce}(z, z^+, z^-) \quad (18)$$

where L represent the layer seleted from the multi-layer of encoder feature. S_l is the number of spatial location in each layer, z represent the anchor embedding from output image. the positive z^+ is the embedding of the corresponding patch from the input image, while the negatives z^- are embeddings of the non-corresponding ones.

The total loss for the USI-GAN is shown as follows:

$$\mathcal{L}_{total} = \lambda_{tscy} \mathcal{L}_{tscy} + \lambda_{cc} \mathcal{L}_{cc} + \mathcal{L}_{odc} + \mathcal{L}_{nce} + \mathcal{L}_{adv} \quad (19)$$

IV. EXPERIMENTS AND RESULTS

A. Datasets

1) *MIST Dataset*: In the MIST dataset [12], there are aligned H&E-IHC patches for four different IHC stains (Ki67, ER, PR, and HER2) critical to breast cancer diagnosis. All patches are of size $1,024 \times 1,024$ and non-overlapping.

2) *IHC4BC*: Similar to the MIST dataset, there are aligned H&E-IHC patches for four different IHC stains (Ki67, PR, HER2, ER) in the IHC4BC dataset. The IHC4BC dataset contains more patches than the MIST dataset, containing approximately 90,000 H&E-IHC pairs. The patch size of these pairs is $1,000 \times 1,000$.

TABLE I
DETAILS OF MIST AND BCI PUBLIC BENCHMARK DATASETS. PAIRED RATE REPRESENT PEARSON-R OF H&E AND WEAKLY PAIRED IHC.

Dataset	Staining Type	No.WSI	No.Pairs (train)	No.Pairs (test)	Paired Rate
MIST	Ki67	56	4,361	1,000	8.50%
	ER	56	4,153	1,000	11.82%
	PR	56	4,139	1,000	11.46%
	HER2	64	4,642	1,000	9.11%
IHC4BC	Ki67	60	17,745	1,000	7.37%
	ER	59	26,395	1,000	16.62%
	PR	60	20,071	1,000	14.09%
	HER2	52	16,995	1,000	16.45%

B. Experimental Settings

Our method is implemented with Python based on PyTorch on a computer with Intel(R) Core(TM) i5-10400 CPU, 48 GB RAM, and a NVidia RTX A6000 GPU. All experiments were conducted with an image resolution of 1024×1024 , and we trained our method with random 512×512 crops. We used 5-layer PatchGAN as the discriminator and ResNet-6Blocks as the generator for our method. For contrastive learning setting, we keep the same with CUT[17], e.g. 256 negative samples, temperature parameter $\tau = 0.07$ for PatchNCE loss. The USIGAN was trained for 80 epochs for MIST and BCI dataset (about 2 days) and 20 epochs for IHC4BC dataset (about 3 days). During training, we used the Adam optimizer with a linear decay scheduler and an initial learning rate of 2×10^{-4} . The hyperparameters in Eq.19 were set as: $\lambda_{tscy} = 10,000$ and $\lambda_{cc} = 10$.

C. Evaluation Metrics

In this work, we employ the following six metrics to evaluate the performance in the synthetic medical images, including the Integrated optical density (IoD), Pearson correlation coefficient (Pearson-R) and F1 score (F1) and Perceptual Hash Value. 1) *IoD*: We processed the generated IHC images and the reference IHC images using Fiji to extract the average fluorescence intensity (Integrated Density, InteDen) for each image to quantitatively evaluate positive stained area between reference and virtual images:

$$IoD \times 10^{-7} = \left| \sum_{i=1}^N \hat{I}_i - \sum_{j=1}^N I_j \right| \quad (20)$$

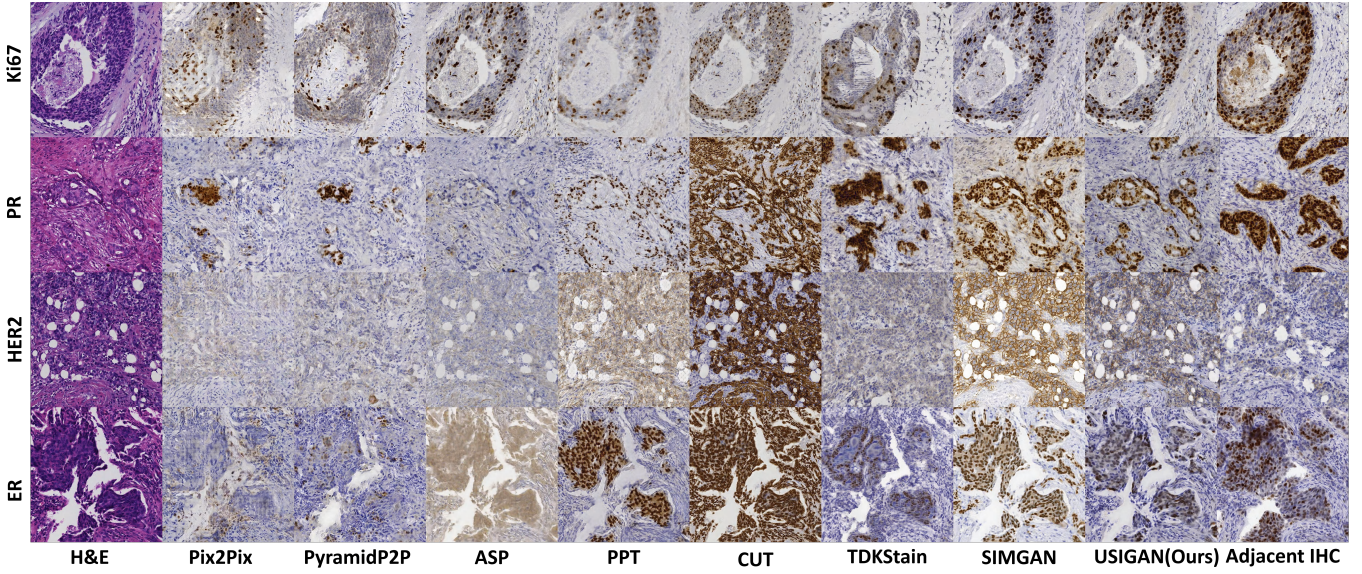


Fig. 4. Selected representative methods exhibit varying performances in virtual IHC staining results visualization on the MIST dataset. The quantitative comparison on different state-of-art methods.

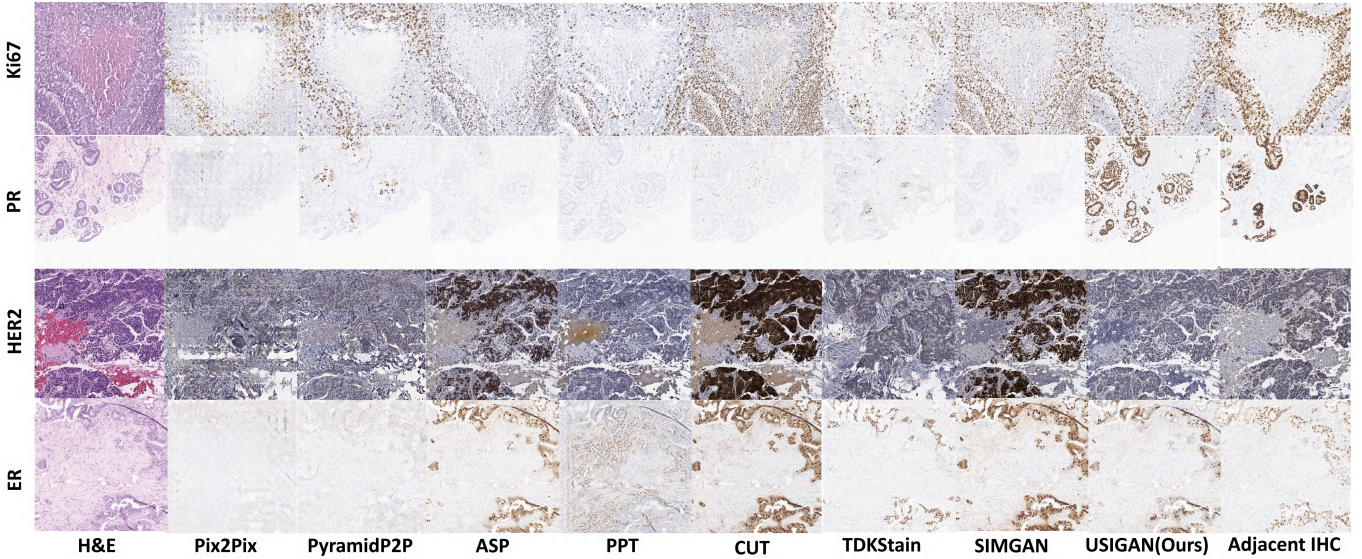


Fig. 5. Selected representative methods exhibit varying performances in virtual IHC staining results visualization on the IHC4BC dataset. The quantitative comparison on different state-of-art methods.

where \hat{I}_i and I_j represents the virtual generated IHC image and Adjacent IHC image Integrated Density. N is the number of test dataset.

2) *Pearson-R*: To quantitatively measure the pathological preserving with adjacent IHC image and content preserving with H&E image we use Pearson-R:

$$R_c = \frac{\sum_{i=1}^N (I_1^{(i)} - \bar{I}_1)(I_2^{(i)} - \bar{I}_2)}{\sqrt{\sum_{i=1}^N (I_1^{(i)} - \bar{I}_1)^2} \sqrt{\sum_{i=1}^N (I_2^{(i)} - \bar{I}_2)^2}} \quad (21)$$

$$R_p = \frac{\frac{1}{N-1} \sum_{i=1}^N (D_i - \bar{D})(O_i - \bar{O})}{\sqrt{\frac{1}{N-1} \sum_{i=1}^N (D_i - \bar{D})^2 \cdot \frac{1}{N-1} \sum_{i=1}^N (O_i - \bar{O})^2}} \quad (22)$$

$$R_{avg} = (R_c + R_p)/2 \quad (23)$$

where R_c and R_p represents content preserving and pathological preserving correlation, respectively. And i is the index of image, N is total numbers of test dataset. $I_1^{(i)}$ and $I_2^{(i)}$ are the grayscale values of the i -th pixel in each image. \bar{I}_1 and \bar{I}_2 are the mean grayscale values of the two images. D_i and O_i represents i -th image Integrated density.

3) *FID*: The Fréchet Inception Distance (FID) is a special GAN metric to measures the quality and diversity of the synthetic images using the pre-trained Inception network, where the lower FID the better performance.

$$FID = \|\mu_r - \mu_g\| + \text{Tr} \left(C_r + C_g - 2(C_r C_g)^{1/2} \right) \quad (24)$$

TABLE II

COMPARISON OF STAIN TRANSFER PERFORMANCE USING DIFFERENT STATE-OF-THE-ART METHODS ON THE MIST BENCHMARK DATASETS. THE BEST AND SECOND BEST SCORES ARE IN **BOLD** AND UNDERLINE, RESPECTIVELY. (THE METRIC LOWER IS BETTER.) R_{avg} IS THE AVERAGE CORRELATION OF PATHOLOGICAL SEMANTICS AND CONTENT. FID FOCUSES MORE ON ASSESSING IMAGE QUALITY, PHV_{avg} ARE MORE CLOSELY TO HUMAN PERCEPTUAL METRIC.

Methods	Ki67			ER			PR			HER2		
	$PHV_{avg}\downarrow$	$R_{avg}(\%)\uparrow$	FID \downarrow									
Pix2Pix [8]	0.4885	37.14	97.347	0.5565	42.39	87.286	0.5181	43.27	81.876	0.5164	37.44	107.403
PyramidP2P [15]	0.5765	35.47	111.514	0.5432	43.73	91.714	0.5465	46.38	92.635	0.5078	38.60	103.068
CycleGAN [31]	<u>0.4747</u>	58.08	33.974	0.4992	63.57	37.438	0.4945	66.23	40.210	0.5053	58.77	54.654
F-LseSim [30]	0.5553	48.06	66.625	0.5451	65.38	143.57	0.5726	63.74	103.67	0.5335	58.27	51.104
CUT [17]	0.5267	64.87	54.420	0.5474	63.43	59.950	0.5559	57.38	59.050	0.5712	57.78	69.550
MoNCE [26]	0.5446	66.26	55.536	0.5430	65.86	59.991	0.5322	69.28	48.560	0.5652	56.44	60.652
QSAtn [7]	0.5468	60.18	49.447	0.5701	65.79	71.653	0.5633	60.09	69.783	0.5632	55.67	65.114
SRC [9]	0.5359	63.60	61.812	0.5615	66.87	55.464	0.5449	72.75	60.305	0.5719	44.46	56.438
UNSB [11]	0.5684	60.30	30.293	0.5603	62.78	34.494	0.5847	61.68	<u>34.895</u>	0.5833	58.36	48.775
PPT [29]	0.5241	51.97	48.640	0.5311	58.13	50.436	0.5232	63.20	50.315	0.5125	55.98	54.384
ASP [12]	0.4922	71.27	44.894	0.5071	74.96	41.400	<u>0.4924</u>	74.34	41.589	0.5020	<u>76.31</u>	47.864
TDKStain [18]	0.4892	42.58	61.982	<u>0.4755</u>	49.66	48.930	0.4929	48.38	57.898	<u>0.4718</u>	44.41	58.638
SIM-GAN [5]	0.5022	<u>73.17</u>	<u>28.518</u>	0.4977	<u>78.27</u>	<u>34.614</u>	0.4995	85.46	35.872	0.5093	73.37	<u>39.665</u>
USI-GAN (ours)	0.4702	<u>77.75</u>	27.363	0.4694	85.07	33.062	0.4560	87.20	34.642	0.4708	83.35	37.765

where μ_r and μ_g are the empirical means of real gaussian variables and synthetic gaussian variables, which are modeled by the pre-trained Inception networks. Likewise, C_r and C_g are the empirical covariance of real gaussian variables and synthetic gaussian variables, respectively.

4) *PHV*: Perceptual Hash Value is describe in [31]. *PHV* evaluates the distribution using multi-level features from a pre-trained network. Compared to FID, which focuses on distribution evaluation, *PHV* places greater emphasis on perceptual aspects in virtual image assessment

D. Comparison with Competitive Methods

We Compare our method with baselines and thirteen state-of-art Image-to-Image translation approaches. It can be divided into the following 2 types:

1. **Image translation SOTA** based on building cross-domain correspondence by contrastive learning, such as: Pix2Pix [8], CycleGAN [31], CUT [17], QSAtn(CVPR'22), MoNCE [26] (CVPR'22), SRC [9] (CVPR'22), LSeSim [30] (CVPR'21), UNSB [11] (ICLR'24).

2. **Virtual staining SOTA methods**, such as: Pyramid-Pix2Pix [15] (CVPR'23), ASP [12] (MICCAI'23), PPT [29] (MICCAI'24), TDKStain [18] (MICCAI'24), SIMGAN [5] (TMI'25).

1) *Results on MIST*: Table II present the quantitative experimental results on the MIST dataset. Our USIGAN exhibits significant advantage on clinical values and image quality. In this table, we report the average values of four key evaluation metrics: pathology-semantic awareness, image quality, content consistency, and pathology-semantic consistency. Our results outperform current state-of-the-art (SOTA) methods across all four staining types: Ki67, HER2, ER, and PR.

The PHV_{avg} metric, the lower the better, which measures the perceived distance between real and generated IHC images in the feature space, serves as a more intuitive indicator of pathology-semantic alignment. This aligns closely with human subjective perceptions, as further corroborated by the subjective evaluation heatmap 10 in the subsequent section. In Figure 6, while USIGAN may not achieve the best performance

in terms of content preservation and pathology-semantic alignment, it demonstrates a balanced performance compared to other methods. For instance, supervised approaches such as TDKStain and PyramidPix2Pix can enforce semantic alignment between generated and real IHC images. However, these methods suffer from lower image quality, higher artifact prevalence, and poor content preservation from H&E images, which significantly limit their clinical applicability. For example, In HER2 Stain experiments, CycleGAN achieve 92.96% in content pearson-R correlation, but its pathology semantic preserving pearson-R correlation only achieve 24.58%. State-of-the-art (SOTA) image translation methods typically excel in content preservation. However, due to the weakly paired nature of the data and the high degree of style-content decoupling in pathological images [25], these methods struggle to establish accurate cross-domain correlations, resulting in low pathology-semantic consistency. Both quantitative and qualitative results confirm the effectiveness of our method in addressing the weakly paired IHC virtual staining.

2) *Results on IHC4BC*: Table III present the quantitative experimental results on the IHC4BC dataset. It is important to emphasize that in the IHC4BC dataset PR sub-dataset, the non-positive regions of pathological images exhibit low contrast and appear nearly transparent, which is easier to classify positive area in OD value. Due to this characteristic, the significant contrast of positive regions in the PR dataset makes global features (such as boundaries and contrast intensity) more critical in the evaluation process. As a result, even though our method achieves high pathological semantic relevance, it does not achieve the best performance in terms of the *PHV* value.

For example, under PR staining, only supervised learning-based methods such as PyramidP2P and Pix2Pix achieve pathological semantic correlations of 66.28% and 40.96%, respectively. In contrast, other advanced CUT-based methods, such as SIMGAN, PPT, and ASP, achieve much lower correlations of 9.10%, 6.66%, and 15.59%, respectively. Notably, our method still achieves a correlation of 36.56%, far surpassing other advanced methods, as shown in Figure 6.

TABLE III

COMPARISON OF STAIN TRANSFER PERFORMANCE USING DIFFERENT STATE-OF-THE-ART METHODS ON THE IHC4BC BENCHMARK DATASETS. THE BEST AND SECOND BEST SCORES ARE IN **BOLD** AND UNDERLINE, RESPECTIVELY. (THE METRIC LOWER IS BETTER.) R_{avg} IS THE AVERAGE CORRELATION OF PATHOLOGICAL SEMANTICS AND CONTENT. FID FOCUSES MORE ON ASSESSING IMAGE QUALITY, PHV_{avg} ARE MORE CLOSELY TO HUMAN PERCEPTUAL METRIC.

Methods	Ki67			ER			PR			HER2		
	$PHV_{avg} \downarrow$	$R_{avg}(\%) \uparrow$	FID \downarrow	$PHV_{avg} \downarrow$	$R_{avg}(\%) \uparrow$	FID \downarrow	PHV_{avg}	$R_{avg}(\%) \uparrow$	FID \downarrow	$PHV_{avg} \downarrow$	$R_{avg}(\%) \uparrow$	FID \downarrow
Pix2Pix [8]	0.4887	40.44	102.77	0.4537	44.96	102.54	0.4837	26.60	215.53	0.5242	47.68	93.70
PyramidP2P [15]	0.4263	48.48	57.24	0.4364	48.78	73.05	0.3951	41.01	62.83	0.5095	45.24	92.52
CycleGAN [31]	0.4248	81.36	39.47	0.4863	69.39	39.04	0.3646	54.22	43.98	<u>0.4662</u>	59.13	53.60
F-LseSim [30]	0.4821	80.94	37.69	0.4683	73.00	61.17	0.4649	47.18	68.77	0.5324	54.81	90.63
CUT [17]	0.4841	<u>82.11</u>	39.05	0.4589	73.63	39.27	0.4095	42.81	42.29	0.5186	66.00	53.14
MoNCE [26]	0.4955	80.84	47.04	46.12	75.81	46.64	0.4805	55.40	72.49	0.5167	64.73	60.06
QSAttn [7]	0.4658	81.69	36.89	0.4637	63.48	39.35	0.4119	48.79	37.01	0.5182	64.11	55.65
SRC [9]	0.4797	81.75	37.36	0.4595	74.09	40.91	0.4454	54.68	37.46	0.5318	63.87	54.74
UNSB [11]	0.4611	78.34	31.81	0.5003	60.03	55.30	0.4502	56.31	37.01	0.5809	56.99	49.04
PPT [29]	0.4539	72.49	54.91	0.5376	20.37	70.91	0.4240	36.83	68.88	0.5298	76.88	56.95
ASP [12]	0.4475	75.22	35.86	0.3751	75.66	39.36	0.4137	51.62	67.65	0.5105	61.00	66.75
TDKStain [18]	0.4185	45.86	57.75	0.4344	43.83	56.47	0.4329	15.82	107.13	0.5082	45.43	66.39
SIM-GAN [5]	0.4934	81.80	38.37	0.4217	80.79	37.93	<u>0.3719</u>	45.23	40.05	0.4396	76.98	58.32
USI-GAN (ours)	0.4064	82.23	23.74	0.3761	82.25	37.01	0.4560	61.80	34.63	0.4611	81.98	48.54

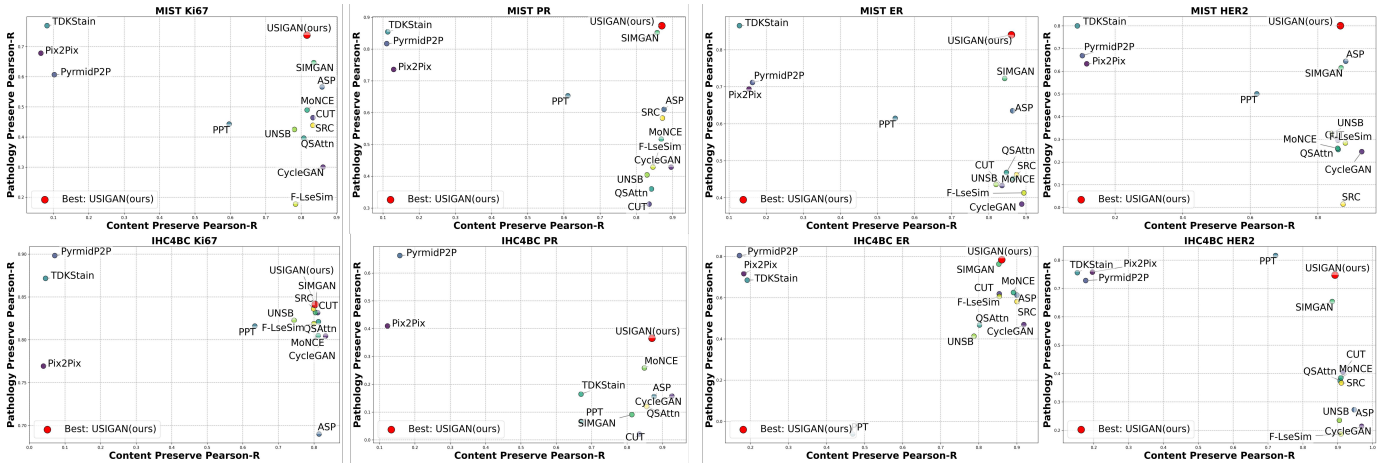


Fig. 6. The visualization results of pathological semantic consistency and content preservation across different methods demonstrate that our approach exhibits outstanding performance in both aspects.

E. Ablation Study and Analysis

1) *Effectiveness of UOT-CTM*: To validate the effectiveness of the proposed cycle-consistent transfer framework and the unbalanced optimal transport strategy, we present Table IV-D2 and Figure 7. We first compared prior works that utilized optimal transport (OT) strategies to constrain the bidirectional mapping between H&E and weakly paired IHC, as well as generated IHC and weakly paired IHC. Additionally, we investigated the effect of adopting an unbalanced optimal transport (UOT) strategy.

The results show that such bidirectional OT constraints lead to a reduction in pathological semantics. However, replacing them with the UOT strategy resulted in significant improvements across multiple metrics, including the total optical density difference (IoD), pathological relevance, image quality, and feature perception score, providing a positive impact over the baseline, as shown in Table IV-D2 \mathcal{L}_1 w (U)OT two column.

Subsequently, we replaced the constraint strategy and incorporated our cycle-consistent strategy based on OT. This approach achieved notable performance gains across all di-

mensions of evaluation metrics. By employing UOT, our method outperformed all experimental groups on every metric, demonstrating its superior effectiveness, as shown in Table IV-D2 \mathcal{L}_{tcyc} w (U)OT two column. In the visualizations shown in Figure 7, our strategy demonstrates the ability to generate staining styles more accurately. In contrast, OT-based methods exhibit overall lower staining contrast in negative regions. Under the same strategy, UOT-based methods achieve greater precision in positive regions.

2) *Effectiveness of PC-SCM*: To explore the effectiveness of PC-SCM and its interaction with UOT-CTM, Table 8 and Table VI present the ablation experiments across all staining types and the ablation study on the combinations of all modules, respectively.

From Table VI, it can be observed that the optical density-based loss L_{odc} achieves the highest improvement in pathological semantic consistency. Meanwhile, the cycle-consistent loss L_{cc} , which serves as a multi-scale feature mining mechanism within the encoder, is influenced by morphological information within the features. However, due to the lack of a prior assumption of morphological consistency across groups in weakly paired data, this results in suboptimal outcomes. When

TABLE IV

COMPARISON OF STAIN TRANSFER PERFORMANCE FOR DIFFERENT METHODS ON THE MIST BENCHMARK DATASETS. THE BEST AND SECOND-BEST SCORES ARE IN **BOLD** AND UNDERLINE, RESPECTIVELY. IO_D, FID AND PHV_{avg} (THE LOWER IS BETTER.)

Methods	Ki67						ER					
	IoD↓	R _c (%)↑	R _p (%)↑	R _{avg} (%)↑	FID↓	PHV _{avg} ↓	IoD↓	R _c (%)↑	R _p (%)↑	R _{avg} (%)↑	FID↓	PHV _{avg} ↓
Baseline	0.4895	77.86	36.34	57.10	27.45	0.5023	0.8598	80.71	42.18	61.44	35.27	0.5103
w/o UOT-CTM	<u>0.2595</u>	80.75	<u>71.81</u>	<u>76.28</u>	29.40	0.5024	1.8404	83.65	<u>81.91</u>	82.78	35.35	0.4662
w/o PC-SCM	0.1915	82.70	44.68	63.69	30.59	<u>0.4977</u>	0.4649	86.35	46.31	66.33	32.84	0.4991
USI-GAN (ours)	0.2680	<u>81.63</u>	73.88	77.75	27.36	0.4702	<u>0.5109</u>	<u>86.06</u>	84.07	85.07	<u>33.06</u>	<u>0.4694</u>

Methods	PR						HER2					
	IoD↓	R _c (%)↑	R _p (%)↑	R _{avg} (%)↑	FID↓	PHV _{avg} ↓	IoD↓	R _c (%)↑	R _p (%)↑	R _{avg} (%)↑	FID↓	PHV _{avg} ↓
Baseline	2.4654	82.06	25.24	53.65	37.97	0.5220	1.7549	85.32	32.80	59.06	42.14	0.5082
w/o UOT-CTM	1.6829	83.53	<u>86.73</u>	<u>85.13</u>	43.40	0.4932	0.7819	84.32	82.94	83.63	37.39	0.4728
w/o PC-SCM	0.4736	87.19	<u>48.90</u>	<u>68.05</u>	34.26	0.5150	1.5598	<u>85.81</u>	21.39	53.60	42.09	0.5247
USI-GAN (ours)	2.0700	87.03	87.37	87.20	<u>34.64</u>	0.456	1.6788	86.63	<u>80.08</u>	<u>83.35</u>	<u>37.76</u>	0.4708

TABLE V

THE QUANTITATIVE COMPARISON RESULTS OF THE EFFECTS OF UOT AND UOT-CTM ON USIGAN. \mathcal{L}_1 w (U)OT REPRESENT CONSTRAIN TRANSPORT STRATEGY BETWEEN $T^{(H-I)}$ AND $T^{(I-I)}$, AND (U)OT REPRESENTS THE THEORY FOR COMPUTING THE COST MATRIX OF FEATURE MATCHING.

Strategy	R _c (%) ↑	R _p (%) ↑	IoD↓	FID↓	PHV _{avg} ↓
baseline	80.71	42.18	0.8590	35.27	0.5103
\mathcal{L}_1 w OT	86.19	37.51	2.5027	33.64	0.5243
\mathcal{L}_1 w UOT	85.69	43.61	2.2763	33.03	0.5042
$\mathcal{L}_{t_{cyc}}$ (OT)	86.25	40.51	1.4186	33.23	0.5084
$\mathcal{L}_{t_{cyc}}$ (UOT)	86.35	46.30	0.4640	32.84	0.4991

TABLE VI

THE ABLATION EXPERIMENTS ON MIST ER FOR ALL MODULES ARE CONDUCTED, WHERE $L_{t_{cyc}}$ REPRESENTS THE UOT-CTM MODULE, AND THE REMAINING COLUMNS REPRESENT THE PC-SCM MODULE.

L_{odc}	L_{cc}	$L_{t_{cyc}}$	R _c (%) ↑	R _p (%) ↑	R _{avg} (%) ↑	FID ↓	PHV _{avg} ↓
-	-	-	80.71	42.18	61.44	35.27	0.5103
✓	-	-	84.06	81.54	<u>82.80</u>	35.16	0.4776
-	✓	-	82.63	75.55	79.09	32.67	0.4908
✓	✓	-	83.65	81.91	81.01	35.35	0.4662
-	-	✓	86.35	46.30	66.33	<u>32.84</u>	0.4991
-	✓	✓	85.88	70.85	78.36	33.05	0.4846
✓	-	✓	85.62	76.58	81.10	33.25	0.5049
✓	✓	✓	<u>86.06</u>	84.07	85.07	33.06	<u>0.4694</u>

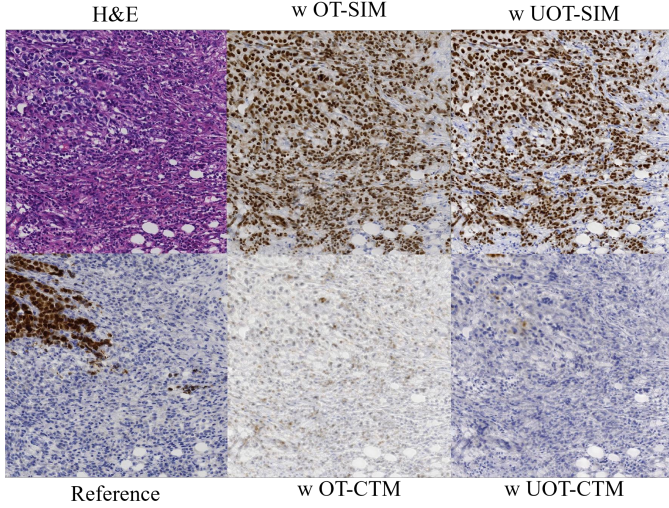


Fig. 7. Visualize the impact of UOT and transport consistency loss compared to the \mathcal{L}_1 loss that directly constrains both transport matrix.

these two components are combined, the shorter gradient back-propagation path of L_{cc} leads to better overall performance.

Additionally, both tables show that UOT-CTM primarily enhances content consistency for H&E images, while PC-SCM significantly improves pathological semantic consistency. When the two are combined, as one focuses on intra-image consistency and the other on inter-image relationships, there is typically a slight reduction in content consistency.

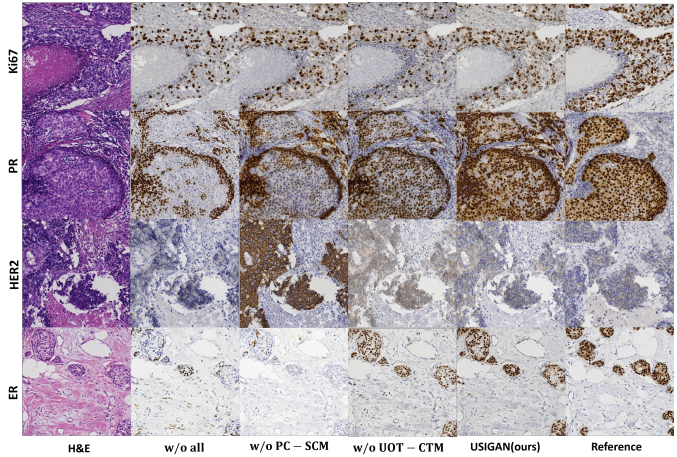


Fig. 8. Visualize the impact of UOT-CTM and PC-SCM on USIGAN on MIST dataset benchmark.

TABLE VII

THE QUANTITATIVE RESULTS OF THE INFLUENCE OF DIFFERENT BATCH SIZE ON THE PERFORMANCE OF THE PC-SCM MECHANISM.

Batch size	R _c (%)	R _p (%)	IoD	FID	PHV _{avg}
1	84.58	23.61	1.9810	47.95	0.5337
2	84.19	57.95	0.8635	49.56	0.5136
4	85.23	57.11	2.1414	49.18	0.5302
8	86.14	57.90	2.6316	57.81	0.5245
16	82.79	61.70	4.0556	64.54	0.5480

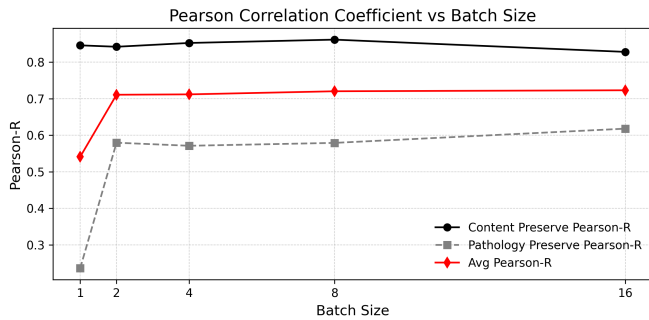


Fig. 9. The influenced different batch size on the Pearson Correlation coefficient between virtual IHC images and adjacent layer real IHC images on PC-SCM mechanism

TABLE VIII

THE QUANTITATIVE RESULTS OF THE INFLUENCE OF DIFFERENT RELAX PARAMETER τ ON THE PERFORMANCE OF THE UOT-CTM MECHANISM ON MIST ER.

τ	$R_c(\%)$	$R_p(\%)$	IoD	FID	PHV _{avg}
0.0001	86.63	52.81	0.4639	57.39	0.5642
0.001	86.35	46.31	0.4649	32.84	0.4991
0.01	87.00	48.41	0.5813	59.18	0.5772
0.1	86.12	42.69	0.5827	58.66	0.5735

However, the average pathological relevance score (R_{avg}) still reaches an optimal level.

3) *Sensitivity to batch size on PC-SCM*: PC-SCM utilizes intra-batch correlation to guide the generated results in maintaining pathological consistency across batches. Therefore, the batch size influences the effectiveness of PC-SCM. To explore the impact of batch size, we set the image reading size to 256 and randomly crop it to 128 for easier requirement of memory. As shown in Table VII The Optical Density vectors, compressed through Focal Optical Density, exhibit increasing instability as the batch size grows. This phenomenon arises due to the weaker direct correlation between morphological features and the intensity values of optical density. As a result, relatively satisfactory results can be achieved at smaller batch sizes, where the impact of this instability is minimized. Overall, a batch size of 4 achieves the best performance by balancing the trade-off between morphological consistency and self-information mining. However, due to the higher computational cost associated with larger batch sizes, we adopt a batch size of 2 as our training configuration. This choice effectively reduces training overhead while maintaining a satisfactory level of performance.

4) *Sensitivity to relax weights on UOT-CTM*: UOT-CTM incorporates a Kullback-Leibler divergence regularization term with a coefficient τ to relax marginal constraints, thereby adapting to weakly paired data. Notably, different values of τ correspond to varying degrees of relaxation, which often yield distinct impacts on model performance. Therefore, investigating the influence of τ values in UOT-CTM is of critical necessity. As τ approaches 0, the optimal transport strategy becomes increasingly consistent with classical optimal transport. Table VIII presents the results of our method using only UOT-CTM-based virtual staining on the ER staining

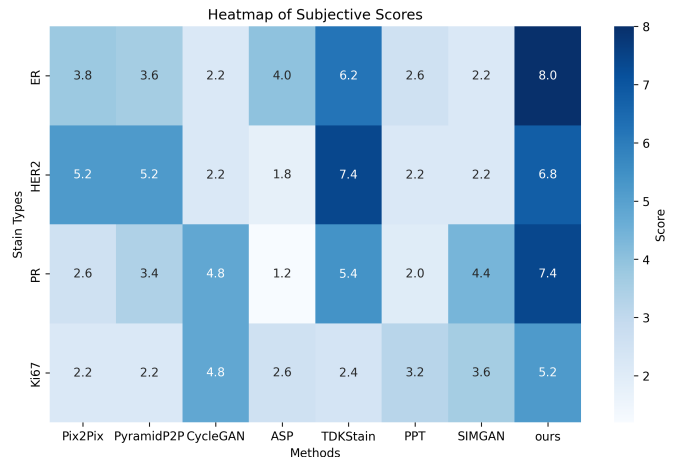


Fig. 10. The heatmap below represents the subjective evaluation scores of pathologists for Immunohistochemistry (IHC) images. These scores were assigned based on their assessment of diagnostic clinical value.

type of the MIST dataset. From the table VIII, the optimal relaxation coefficient is inferred to lie between 0.01 and 0.0001. It reveals that as the relaxation coefficient (τ) decreases, the pathological relevance of the generated images increases. However, when the relaxation degree is excessively low, inaccurate transport strategies lead to erroneous feature matching, thereby degrading image quality. Conversely, when the relaxation degree is excessively high, the uncertainty in the mapping relationship between morphological information and staining style intensifies, resulting in declines in both image quality and pathological relevance. In our experiments, we determined that the optimal relaxation coefficient is 0.001, under which our USIGAN achieves its best performance.

F. Subjective Evaluation

In this study, we randomly selected 10 virtually generated images per staining type from the IHC4BC and MIST test datasets, created using our proposed method. A panel of experienced pathologists evaluated these images based on their diagnostic value compared to adjacent real IHC slices, focusing on alignment with pathological features critical for clinical decision-making, as shown in Figure 10.

The results showed that our method outperformed state-of-the-art (SOTA) approaches in diagnostic utility and consistency with real IHC characteristics across all staining types. While TDKStain achieved the highest HER2 staining score due to its posterior constraints on cell density, its poor preservation of H&E content limited its clinical applicability. In contrast, our method excelled in both content preservation and pathological alignment, demonstrating strong potential for clinical and research applications, as shown in Figure 6.

V. DISCUSSION

A. Why Pearson-R? Why not SSIM / PSNR?

Previous studies often relied on SSIM and PSNR to evaluate the quality of generated results; however, these metrics are scientifically inadequate for assessing diagnostic value in

pathological images. For weakly paired data, pixel-level differences fail to capture the pathology-relevant features. As shown in Table IX, comparisons using the IHC4BC dataset reveal that pixel-level metrics vary significantly across datasets with different pairing degrees (see Table IV-A2). Notably, similar SSIM scores can correspond to vastly different pathology-semantic correlations. For instance, in the PR staining type, PyramidP2P and PPT methods achieve correlations of 66.28% and 6.66%, respectively. To address these limitations, we adopt a clinically relevant evaluation approach, focusing on the correlation between optical density and pathological positivity intensity. This method better reflects the diagnostic utility of generated results, emphasizing their value for clinical applications.

TABLE IX
DISCUSSION ABOUT SSIM AND PSNR METRIC ON IHC VIRTUAL STAINING ON IHC4BC DATASET

Method	PR			HER2		
	SSIM	PSNR	$R_p(\%)$	SSIM	PSNR	$R_p(\%)$
Pix2Pix [8]	0.5038	23.083	40.96	0.1248	11.3663	75.76
PyramidP2P [15]	0.5258	<u>23.9905</u>	66.28	0.1162	11.1824	72.79
CycleGAN [31]	<u>0.5546</u>	23.2907	15.76	<u>0.128</u>	10.9497	21.40
F-LseSim [30]	0.4976	20.4933	12.59	0.1275	10.8599	18.69
CUT [17]	0.5452	23.3178	2.13	0.1214	10.6364	40.47
MoNCE [26]	0.4845	18.9298	25.88	0.1175	10.3727	38.54
QSAtn [7]	0.5449	23.3068	12.01	0.1228	10.8112	37.54
SRC [9]	0.4989	21.1762	54.68	0.1229	10.7725	36.70
UNSB [11]	0.511	23.7755	56.31	0.1087	11.1355	23.51
PPT [29]	0.529	23.3723	6.66	0.1339	11.38007	81.60
ASP [12]	0.5762	24.4079	15.59	0.1202	10.9916	27.24
TDKStain [18]	0.4998	23.3719	16.46	0.1275	10.9003	75.58
SIMGAN [5]	0.5247	21.999	9.10	0.12	10.702	65.38
USIGAN(ours)	0.2163	14.2176	36.57	0.1267	11.1342	74.76

VI. CONCLUSION

In this paper, we propose a GAN-based H&E-to-IHC staining transfer model for self-information mining, named USIGAN. A key challenge in this process is the absence of pixel alignment during training, which makes it difficult to ensure pathological expression consistency with adjacent slices and maintain high content consistency with H&E images. To address these issues, we incorporate two novel mechanisms into USIGAN: the Unbalanced Transport Consistency (UOT-CTM) mechanism and the Pathology Self-Correspondence Consistency (PC-SCM) mechanism. Despite the satisfactory results achieved by USIGAN, it requires separate training for each staining type, leading to inconsistent performance across different staining types, which will be a focus of future optimization. Moreover, compared to similar methods, USIGAN has a larger number of parameters and slower training speed. This is mainly due to the computational demands of calculating the optimal transport cost matrix. We hope that future research will develop lighter and more accurate computational methods to address this issue. We will continue to explore more lightweight transport approaches and more rigorous theoretical derivations to develop virtual staining methods for self-information mining.

VII. ACKNOWLEDGEMENTS

This work was supported in part by the National Natural Science Foundation of China (No. 62271475), Ministry

of Science and Technology's key research and development program (2023YFF0723400), Shenzhen-Hong Kong Joint Lab on Intelligence Computational Analysis for Tumor Imaging (E3G111), and the Youth Innovation Promotion Association CAS (2022365).

REFERENCES

- [1] Fuqiang Chen et al. "Pathological semantics-preserving learning for H&E-to-IHC virtual staining". In: *International Conference on Medical Image Computing and Computer-Assisted Intervention*. Springer, 2024, pp. 384–394.
- [2] Lenaic Chizat et al. "Scaling algorithms for unbalanced transport problems". In: *arXiv preprint arXiv:1607.05816* (2016).
- [3] B DoanNgan, DarrowMorgan Angus, LeeHan Sung, et al. "Label-free virtual HER2 immunohistochemical staining of breast tissue using deep learning". In: *BME frontiers* (2022).
- [4] Aritra Ghosh and Andrew Lan. "Contrastive learning improves model robustness under label noise". In: *Proceedings of the IEEE/CVF conference on computer vision and pattern recognition*. 2021, pp. 2703–2708.
- [5] Xianchao Guan et al. "Supervised Information Mining from Weakly Paired Images for Breast IHC Virtual Staining". In: *IEEE Transactions on Medical Imaging* (2025).
- [6] K de Haan et al. *Deep learning-based transformation of H&E stained tissues into special stains*. *Nat Commun*. 2021; 12: 4884.
- [7] Xueqi Hu et al. "Qs-attn: Query-selected attention for contrastive learning in i2i translation". In: *Proceedings of the IEEE/CVF Conference on Computer Vision and Pattern Recognition*. 2022, pp. 18291–18300.
- [8] Phillip Isola et al. "Image-to-image translation with conditional adversarial networks". In: *Proceedings of the IEEE conference on computer vision and pattern recognition*. 2017, pp. 1125–1134.
- [9] Chanyong Jung, Gihyun Kwon, and Jong Chul Ye. "Exploring Patch-Wise Semantic Relation for Contrastive Learning in Image-to-Image Translation Tasks". In: *Proceedings of the IEEE/CVF Conference on Computer Vision and Pattern Recognition (CVPR)*. June 2022, pp. 18260–18269.
- [10] Chanyong Jung, Gihyun Kwon, and Jong Chul Ye. "Exploring patch-wise semantic relation for contrastive learning in image-to-image translation tasks". In: *Proceedings of the IEEE/CVF conference on computer vision and pattern recognition*. 2022, pp. 18260–18269.
- [11] Beomsu Kim et al. *Unpaired Image-to-Image Translation via Neural Schrödinger Bridge*. 2024. arXiv: 2305.15086 [cs.CV]. URL: <https://arxiv.org/abs/2305.15086>.
- [12] Fangda Li et al. "Adaptive supervised patchnce loss for learning h&e-to-ihc stain translation with inconsistent groundtruth image pairs". In: *International Conference on Medical Image Computing and Computer-Assisted Intervention*. Springer, 2023, pp. 632–641.

- [13] Jia-Ren Lin et al. “High-plex immunofluorescence imaging and traditional histology of the same tissue section for discovering image-based biomarkers”. In: *Nature cancer* 4.7 (2023), pp. 1036–1052.
- [14] Xiaoqi Lin. “Characteristic morphology and immunohistochemical patterns of clear cell papillary renal cell tumours may be observed in renal cell carcinomas, a critical pitfall in renal biopsy cytopathology”. In: *Cytopathology* 35.4 (2024), pp. 481–487.
- [15] Shengjie Liu et al. “Bci: Breast cancer immunohistochemical image generation through pyramid pix2pix”. In: *Proceedings of the IEEE/CVF conference on computer vision and pattern recognition*. 2022, pp. 1815–1824.
- [16] Shuting Liu et al. “Unpaired stain transfer using pathology-consistent constrained generative adversarial networks”. In: *IEEE transactions on medical imaging* 40.8 (2021), pp. 1977–1989.
- [17] Taesung Park et al. “Contrastive learning for unpaired image-to-image translation”. In: *Computer Vision—ECCV 2020: 16th European Conference, Glasgow, UK, August 23–28, 2020, Proceedings, Part IX 16*. Springer. 2020, pp. 319–345.
- [18] Qiong Peng et al. “Advancing H&E-to-IHC Virtual Staining with Task-Specific Domain Knowledge for HER2 Scoring”. In: *International Conference on Medical Image Computing and Computer-Assisted Intervention*. Springer. 2024, pp. 3–13.
- [19] Yair Rivenson et al. “Virtual histological staining of unlabelled tissue-autofluorescence images via deep learning”. In: *Nature biomedical engineering* 3.6 (2019), pp. 466–477.
- [20] Arnout C Ruifrok, Dennis A Johnston, et al. “Quantification of histochemical staining by color deconvolution”. In: *Analytical and quantitative cytology and histology* 23.4 (2001), pp. 291–299.
- [21] Tehrani. “Nonlinear imaging histopathology: a pipeline to correlate gold-standard hematoxylin and eosin staining with modern nonlinear microscopy”. In: *IEEE Journal of Selected Topics in Quantum Electronics* 29.4: Biophotonics (2023), pp. 1–8.
- [22] Frency Varghese et al. “IHC Profiler: an open source plugin for the quantitative evaluation and automated scoring of immunohistochemistry images of human tissue samples”. In: *PloS one* 9.5 (2014), e96801.
- [23] Ting-Chun Wang et al. “High-resolution image synthesis and semantic manipulation with conditional gans”. In: *Proceedings of the IEEE conference on computer vision and pattern recognition*. 2018, pp. 8798–8807.
- [24] Weilun Wang et al. “Instance-wise hard negative example generation for contrastive learning in unpaired image-to-image translation”. In: *Proceedings of the IEEE/CVF international conference on computer vision*. 2021, pp. 14020–14029.
- [25] Bing Xiong et al. “Unpaired Multi-Domain Histopathology Virtual Staining using Dual Path Prompted Inversion”. In: *Proceedings of the AAAI Conference on Artificial Intelligence*. Vol. 39. 8. 2025, pp. 8780–8787.
- [26] Fangneng Zhan et al. “Modulated contrast for versatile image synthesis”. In: *Proceedings of the IEEE/CVF Conference on Computer Vision and Pattern Recognition*. 2022, pp. 18280–18290.
- [27] Fangneng Zhan et al. “Unbalanced feature transport for exemplar-based image translation”. In: *Proceedings of the IEEE/CVF conference on computer vision and pattern recognition*. 2021, pp. 15028–15038.
- [28] Ranran Zhang et al. “MVFStain: multiple virtual functional stain histopathology images generation based on specific domain mapping”. In: *Medical Image Analysis* 80 (2022), p. 102520.
- [29] Wei Zhang et al. “High-Resolution Medical Image Translation via Patch Alignment-Based Bidirectional Contrastive Learning”. In: *International Conference on Medical Image Computing and Computer-Assisted Intervention*. Springer. 2024, pp. 178–188.
- [30] Chuanxia Zheng, Tat-Jen Cham, and Jianfei Cai. *The Spatially-Correlative Loss for Various Image Translation Tasks*. 2021. arXiv: 2104.00854 [cs.CV]. URL: <https://arxiv.org/abs/2104.00854>.
- [31] Jun-Yan Zhu et al. “Unpaired image-to-image translation using cycle-consistent adversarial networks”. In: *Proceedings of the IEEE international conference on computer vision*. 2017, pp. 2223–2232.